Direct Measurements of Ice-Shelf Flexure caused by Surface Meltwater Ponding and Drainage

Alison F. Banwell[1,2*], Ian C. Willis[2,1], Grant J. Macdonald[3], Becky Goodsell[3] & Douglas R. MacAyeal[3]

1. *Scott Polar Research Institute (SPRI), University of Cambridge, Cambridge, UK. *email: alison.banwell@colorado.edu.*

2. *Cooperative Institute for Research in Environmental Sciences (CIRES), University of Colorado Boulder, Boulder, CO, USA.*

3. *Department of the Geophysical Sciences, University of Chicago, Chicago, IL, USA.*

Abstract

Global sea-level rise is caused, in part, by more rapid ice discharge from Antarctica, following the removal of the restraining forces of floating ice-shelves after their break-up. A trigger of ice-shelf break-up is thought to be stress variations associated with surface meltwater ponding and drainage, causing flexure and fracture. But until now, there have been no direct measurements of these processes. Here, we present field data from the McMurdo Ice Shelf, Antarctica, showing that the filling, to ~2 m depth, and subsequent draining, by overflow and channel incision, of four surface lakes causes pronounced and immediate ice-shelf flexure over multiple-week timescales. The magnitude of the vertical ice-shelf deflection reaches maxima of ~1 m at the lake centres, declining to zero at distances of <500 m. Our results should be used to guide development of continent-wide ice-sheet models, which currently do not simulate ice-shelf break-up due to meltwater loading and unloading.

Introduction

Surface meltwater lakes, together with stream and river networks have been widespread on the floating ice shelves that surround the Antarctic continent for decades[1-6]. Lakes are thought to be hazardous to ice-shelf stability by acting as concentrated loads that flex and weaken the floating ice[2-5,7-12]. Surface streams and rivers facilitate the movement of meltwater across ice-shelves[3,6], and therefore have an important role in controlling lake filling and draining[3,5]. When meltwater is simply produced and then re-frozen in-situ, there is no mass change at the surface. Numerical model and laboratory simulations suggest that if meltwater is advected across the ice-shelf surface, causing lakes to fill and drain (resulting, respectively, in local loading and unloading of the surface), the ice-shelf will flex, which may lead to the formation of fractures both within and outside the lake basins[10,13]. A modelling study has suggested that if these fractures intersect other nearby lake basins, a chain reaction of further lake-drainage events may be initiated, potentially contributing to large-scale ice shelf break-up[10]. This scenario is supported by remote-sensing observations of the break-up of the Larsen B Ice Shelf in 2002[1,14]. Ice shelves that have undergone significant thinning due to surface ablation and ocean-driven ablation at the ice-shelf base[15-18] may be particularly vulnerable to break-up[10,14,19].

38 Although the effects of surface lakes on ice-shelf flexure, fracture and stability have been
39 simulated by small-scale laboratory experiments and theoretical models[9-12,20], there are currently
40 no field data confirming whether ice-shelf flexure (and potential fracture) in response to meltwater
41 movement, ponding or draining actually occurs. Therefore, the aim of the present study was to
42 collect field measurements to examine this process. The key practical constraint on our field
43 campaign was to find a suitable location to collect the data. Given the remoteness of most
44 presently melting Antarctic ice shelves, we undertook our study at the best site available; on the
45 McMurdo Ice Shelf (McMIS) near the logistical hub of McMurdo Station (Fig. 1).

46 The McMIS is a small (~1500 km^2) portion of the Ross Ice Shelf (Fig. 1). Parts of its surface are
47 covered by large quantities of fine debris[21], most of which was transported into the area by a large
48 ice sheet/shelf system at the Last Glacial Maximum, and is now exposed on the surface due to
49 surface ablation that is balanced by basal freezing of marine ice[22]. This debris gives the surface a
50 low albedo, which facilitates surface and shallow subsurface melting[23] despite McMIS being
51 relatively far south (~77°). Surface ablation is further enhanced due to the relatively warm
52 prevailing south-westerly winds, which warm adiabatically as they descend onto the McMIS from
53 the nearby landmasses of Minna Bluff and Mount Discovery[22]. Our ~40 km^2 study site is located <
54 5 km from the calving front where the ice shelf is relatively thin (10 - 30 m, refs 23, 24) (Fig. 1a).
55 Within this area, we measured a mean surface melt rate of 5.2 mm w.e. day^{-1} against 12 ablation
56 stakes (range = 1.0 – 20.6 mm) from early November 2016 to late January 2017. The high surface
57 ablation rates and shallow ice depths gave us a good chance of measuring significant changes in
58 vertical ice deflection rates in response to variations in surface meltwater ponding and draining.

59 Here, we present field observations from in and around four meltwater lakes from early November
60 2016 to late January 2017 (Methods). These observations include data from twelve differential
61 global positioning system (GPS) stations (three per lake site, mounted on poles drilled into the ice,
62 in a ~1 - 1.5 km transect extending outwards from each lake centre) and eight water pressure
63 sensors, two or three per lake site (Fig. 1b). Combined, these are the first direct measurements of
64 ice-shelf flexure in response to the filling and draining of surface meltwater lakes. We show that
65 changes in surface lake volumes cause immediate and pronounced ice-shelf flexure; the magnitude
66 of vertical ice motion decreases as a function of distance from the maximum change in meltwater
67 loading. Our field data are supported by an exact analytic solution for flexure of a floating, thin
68 elastic plate, in which constrained parameter values fall within sensible ranges.

Results

Active meltwater lakes versus relict frozen lake scars

71 Fieldwork survey corroborated by analysis of satellite-imagery from the previous 18 years
72 suggests that active meltwater lakes on the McMIS form in topographically low areas with high
73 debris concentrations, e.g. Peanut, Ring, Rift Tip and Wrong Trousers (hereafter WT) lakes (Figs.
74 1b and 2, where at each site, GPS 1 is closest to the lake centre, and GPS 3 is furthest away). The
75 low albedo of the debris, much of which appears to enter the lake basins entrained by inflowing
76 meltwater, enhances melt rates, as does the relatively low albedo of the ponded meltwater
77 compared to the surrounding bare ice[22].

78 In addition to the active lakes that fill and drain during the melt season, relict, frozen lake scars are

79   also present, and remain almost entirely frozen at their surface year-round due to their relatively
80   high surface albedo. Good examples of these features are the areas where Ring and Peanut GPS 3s
81   are located (Figs. 1b and 2). Low surface melt rates in these areas, combined with vertical
82   hydrostatic adjustments made by the floating ice-shelf, mean that the frozen lake scars appear as
83   raised pedestals compared to the surrounding topography. Meltwater, therefore, often pools to
84   form active meltwater lakes in the topographically-low areas around the pedestalled, relict lake
85   scars (e.g. where Ring and Peanut GPS 1s are located; Figs. 1b and 2).

86   **Ice-shelf vertical elevation change observations**

87   At all lake sites during the melt season, the greatest changes in ice-shelf vertical elevation in
88   response to meltwater loading/unloading are close to the active lake centres (i.e. at each GPS 1).
89   The data from all four GPS transects support this (Figs. 3 and 4). Data from GPS 1 at all lake sites
90   apart from the Peanut site (where we have no measured water depth data near to GPS 1), also show
91   that there is a clear coincidence between the time periods when lake depths are increasing and
92   when the ice shelf is deflecting vertically downward (Figs. 3 and 4). These temporal coincidences
93   occur immediately before GPS 1 at each lake site reaches its lowest elevation (indicated by a red
94   dot below the red lines, Figs. 3 and 4, top plots), and is clearest at Ring GPS 1 between 21 and 22
95   December (Fig. 3a, top plot). There is also a clear temporal coincidence between the initiation of
96   vertical uplift at Ring and WT GPS 1s, and the initiation of the Ring and WT lake drainages (Figs.
97   3a and 4a). The same cannot be said at Rift Tip or Peanut due to missing GPS data at Rift Tip and
98   a lack of water depth data at Peanut (Figs. 3b and 4b).

99   Data from the Ring site show the most pronounced example of the immediate vertical ice
100   movement in response to the filling and draining of a lake (Fig. 3a). Until mid-December, Ring
101   GPS 1 uplifts slowly at ~3 mm day^{-1}, equal to the mean seasonal uplift rate of Ring GPS 2 and 3.
102   This steady uplift is the background trend observed at all 12 GPS stations during the melt season
103   and is likely due to relatively high surface meltwater production and export rates, compared to low
104   meltwater import and ponding rates, causing the ice shelf to uplift hydrostatically as it experiences
105   a net loss of surface mass (see Net meltwater budget calculations section, below, for further
106   analysis and explanation). This upward deflection trend, indicative of net unloading from the area,
107   suggests that the majority of the meltwater that slowly fills Ring lake until mid-December is
108   produced in-situ, as opposed to being transported in from the surrounding area via surface melt
109   streams. Thus, although Ring lake fills between late November and mid-December, the dominant
110   trend of Ring GPS 1 is uplift as more mass is being lost from the area near to Ring GPS 1 by
111   meltwater production and export than is being transported into the area and is ponding.

112   However, from ~14 December, when Ring lake fills more quickly, the dominant trend of Ring
113   GPS 1 is downward deflection, at ~10 mm day^{-1}. Between 21 and 22 December, Ring GPS 1 goes
114   down rapidly by ~0.2 m, corresponding to the time when the lake fills most rapidly and reaches >
115   2 m in depth. The downward deflection measured between 14 and 22 December is indicative of net
116   loading in the vicinity of Ring GPS 1, suggesting that inflow of meltwater from the surrounding
117   area is now contributing to the filling of Ring lake. On 22 December, Ring lake starts to drain and
118   Ring GPS 1 immediately starts to rise rapidly by ~50 mm day^{-1}. In total, Ring GPS 1 rises by 0.96
119   m between 22 December and 28 January (Fig 3a, top plot).

120   The data from Rift Tip GPS 1 also show a pronounced uplift response to lake drainage (Fig. 3b),

121 but due to missing data (dashed red line), the precise uplift initiation date is unknown. If the uplift
122 response was as fast as it was at Ring, then uplift initiation was likely to be on or around 15
123 December, as our Rift Tip water-pressure sensor data (Fig. 3b) and evidence from a time-lapse
124 movie of Rift Tip lake filling and draining (produced from photos taken at 30-minute intervals,
125 Supplementary Movie 1) shows Rift Tip lake started to drain on 15 December (Supplementary
126 Fig. 1b). The movie also shows that Rift Tip lake drains via surface overflow in ~9 days, assisted
127 by the incision of a surface stream (Supplementary Fig. 1c), which drains water from ~22
128 December onwards. As we have no field evidence of hydrologically-induced cracks or moulins,
129 and as the drainage times for the three other lakes was also of the order of days (i.e. longer than the
130 typical time taken for drainage by hydrofracture[23,24]), we assume that they also drain slowly by
131 overflow (e.g., by removal of a natural impediment and/or channel incision at the lake outflow).

132 **Net meltwater budget calculations**

133 The net meltwater budgets, each defined as the meltwater ponding volume (calculated from
134 Landsat 8 satellite imagery analysis) minus the total meltwater production volume (calculated by a
135 positive degree-day (PDD) model) between early November and late January, within a circle of
136 radius (r) 250 m centred on each of the 12 GPSs (Fig. 1b, and Methods), were calculated in order
137 to help explain the vertical movements of each GPS station. Our results show that the seasonal net
138 meltwater budgets at all GPS stations, each defined as the maximum minus minimum net
139 meltwater budget during the 2017/2017 melt season, are negative (Figs. 3 and 4). This is indicative
140 of a net mass loss from each of these 12 areas during the melt season, due to a greater volume of
141 meltwater production (and export), than of meltwater ponding (and import), and explains the
142 dominant uplift signal at all GPS stations through the majority of the melt season (varying between
143 3 – 10 mm day^{-1} for all GPSs 2 and 3; Figs. 3 and 4). The mass that is lost, i.e. meltwater, is
144 transported either to other areas of the ice shelf or, more likely, to the ocean via surface streams.
145 Some of the measured vertical uplift may be partially attributable to sub-ice-shelf accumulation,
146 but as surface ablation is balanced by sub ice-shelf accumulation on an annual basis[22], and as
147 surface melting is most prevalent in the summer, we deduce that surface melting is likely the
148 dominant control on ice-shelf uplift change during the summer melt season.

149 We also note that the short-lived reduction in the uplift rate around 5/6 January in all GPS datasets
150 (Figs. 3 and 4) is likely due to a snow-fall event, evidence of which is shown in Supplementary
151 Movie 1. This snow-fall event would have temporarily added a small load to the ice-shelf surface
152 and, perhaps more importantly, would have increased the surface albedo (and thereby reduced
153 meltwater production rates) and increased surface meltwater storage in the snow (and thereby
154 reduced meltwater export rates).

155 For both the Ring and Peanut sites, the locations with the greatest change in the net meltwater
156 budget over the season correspond with the places that experience the greatest total change in
157 vertical ice elevations i.e. at Ring and Peanut GPS 1s (Figs. 3a and 4b). For example, Ring GPS 1,
158 which undergoes the greatest total change in vertical elevation (~1 m) out of all GPS 1s, also
159 experiences the greatest total seasonal net meltwater budget change in its surrounding area (Fig.
160 3a). There, the net meltwater budget is greatest (4.1 x 10^4 m^3) on 24 December, coinciding with
161 the time when Ring GPS 1 is at its lowest elevation, and smallest (-1.6 x 10^4 m^3) on 18 January,
162 when Ring GPS 1 is close to its highest elevation. The net removal of water from the r = 250 m

4

163 circular area centred on Ring GPS 1 between those dates is 5.7 x 10^4 m^3 (Fig. 3a); a volume that
164 we refer to as the seasonal net meltwater budget. It is not possible to identify a similar
165 correspondence between the maximum changes in meltwater budget and ice elevation at the Rift
166 Tip and WT sites (Figs. 3b and 4a). However, for both the Rift Tip and WT GPS transects, the
167 seasonal changes in net meltwater budgets are more similar across each transect (i.e. between the
168 three GPS stations), than they are at the Ring and Peanut sites.

169 **Analytic expression for idealised ice-shelf flexure**

170 Compared to the GPS 1 station data, which record pronounced vertical movement at the centre of
171 all lake sites, GPSs 2 and 3 are distal from the lake centres and generally do not show a
172 pronounced response to lake filling or drainage (Figs. 3 and 4). The exception to this is Rift Tip
173 GPSs 2 and 3, which are both < 250 m of Rift Tip GPS 1 and uplift vertically at a rate that is
174 almost as rapid as that measured at GPS 1 when Rift Tip lake drains (Fig 3b). Therefore, the data
175 from all sites suggests that the flexural responses to load changes are local (e.g. < 500 m from lake
176 centres). An exact analytic solution for removal of a disk-shaped load from a thin elastic-plate[10]
177 (Methods) supports this observation. For example, using a combination of constrained parameter
178 values that produce the best match between the analytic solution and measured deflection at Ring
179 lake's centre (see below and Methods), its centre is simulated to rise by ~1 m, whereas the ice
180 surface > 250 m away from the lake centre rises by < 10 mm (Fig. 5a). Our field measurements at
181 Ring GPSs 2 and 3 record some net uplift during the season (80 mm and 70 mm, respectively), but
182 this is due to the slightly negative seasonal net meltwater budget at each of these locations (Fig.
183 3a).

184 The parameters in the analytic solution deemed to be most sensitive are lake radius (R); effective
185 ice thickness (H); and Young's Modulus (E). Sensitivity tests were run for varying combinations
186 of values for these parameters within the following ranges: R = 50 – 250 m; H = 10 – 30 m; and E
187 = 1 – 10 GPa. These ranges are guided by: our field data (R); McMIS data collected by others
188 (H)[24,25]; and, values derived through modelling and laboratory experiments by others (E)[10,11,29].
189 For Ring lake, calculated centre-lake deflection and maximum von-Mises stress for varying
190 combinations of values for the parameters R, H and E are given in Supplementary Table 1.
191 Optimal values of these parameters for Ring lake, where our net meltwater budget calculations
192 show that a meltwater volume of 5.7 x 10^4 m^3 is removed during the melt season, are found to be
193 125 m, 10 m, and 1 GPa, respectively (Fig. 5a), giving the ~ 1 m uplift at Ring lake's centre that is
194 consistent with our GPS 1 measurements (Fig. 3a).

195 The optimal values of H (10 m) and E (1 GPa) established for Ring Lake were then used within
196 the analytic solution and applied to the other three lakes to see if the analytic solution agreed with
197 GPS 1 vertical elevation data measured there. The other lakes have different meltwater unloading
198 inputs, as indicated by our seasonal net meltwater budget calculations (Figs. 3 and 4, lower three
199 plots in each), thus we expected that changing the value of R for each lake would be necessary.
200 Agreement between the simulated and measured centre-lake deflections was obtained with R
201 values of 250 m, 175 m, and 200 m for Rift Tip, WT and Peanut lakes, respectively
202 (Supplementary Fig. 2), which are plausible based on our field and satellite-based observations.
203 With these parameter values, the ice surface is simulated to rise by < 10 mm at distances of > 370
204 m, > 284 m, and > 302 m away from the centres of Rift Tip, WT and Peanut lakes, respectively.

205   Therefore, as with the results for Ring lake, the results for the other three lakes show that
206   meltwater loading/unloading has only a local flexural effect (Supplementary Fig. 2). At Rift Tip,
207   GPSs 2 and 3 are < 370 m away from Rift Tip lake centre, so some of their observed uplift is
208   explained by the net meltwater unloading at GPS 1, with the rest due to meltwater unloading
209   closer to those stations (Fig. 3b, Supplementary Fig. 2a). Similarly, WT and Peanut GPS 2s are,
210   respectively, < 284 m and < 302 m away from their respective lake centres, but their GPS 3s lie
211   further away. The measured deflections at their GPS 3s is due entirely to the net meltwater
212   unloading close to those stations; at their GPS 2s it is due mainly to local unloading, with a small
213   fraction in response to unloading at their GPS 1 sites (Figs. 4a and b, Supplementary Figs. 2b and
214   c).

Discussion

216   While lake filling and, more significantly, drainage, caused differential changes in local ice-shelf
217   elevation, and therefore ice flexure, across all four of our lake sites, no observable fractures
218   formed. It is reasonable to expect that: hydrofracture does not assist flexure-driven fracture when
219   ice-shelf thicknesses are small, because the hydrostatic head can never become large enough[30];
220   and/or lakes on the McMIS simply do not currently reach large enough volumes to produce
221   sufficient tensile-stress levels for fracture initiation[10,31]. Small lake volumes may be attributable to
222   the low amplitude of surface topographic undulations, which means that lakes drain via surface
223   overflow after reaching just a small water volume. An extensive stream/river system may help
224   lakes to drain by overflow, and may also intercept and evacuate meltwater before it is ever able to
225   enter potential lake basins. Much of this meltwater will be transported off the ice shelf and into the
226   ocean[32,33], thereby contributing to the ice shelf's negative seasonal net meltwater budget.
227   Alternatively, local flexure-induced tensile stresses alone (Fig. 5b, Supplementary Fig. 2) may be
228   sufficiently large for fracture, but stresses from further afield, such as back-stresses from land-fast
229   sea ice[34] and/or stresses from larger-scale ice-flow[35], may be acting to prevent fracture initiation[5].

230   Although our results indicate that there is currently a negative net meltwater budget on the McMIS
231   during the melt season, melt rates on many of Antarctica's ice shelves are expected to increase
232   two- to three-fold by 2050[36]. Therefore, meltwater volumes may become so great that even if
233   large-scale river systems develop to evacuate meltwater off the ice shelves and into the ocean[33],
234   their discharge capacity may be insufficient to prevent positive net meltwater budgets developing
235   during a melt season (or over successive seasons)[32,33]. Such increased meltwater loading may
236   increase the potential for fracture formation, and ultimately, ice-shelf break-up, perhaps once a
237   given ponding density threshold is exceeded[8]. Surpassing a given ponding density may also enable
238   a chain-reaction style lake drainage process to assist with ice-shelf break-up[5,10]. Currently on the
239   McMIS, surface lakes are not sufficiently widespread for the localized meltwater-loading induced
240   flexure (and potential fractures) to affect more than one lake. Other ice shelves that are already
241   experiencing more widespread melting and pond formation[2-] may be more vulnerable to break-up[5].

242   The results of this study, which are based on field measurements, show that surface meltwater
243   ponding and drainage has a prominent and instantaneous effect on ice-shelf vertical deflection and
244   flexure. The magnitude of the vertical ice-shelf deflection decreases from maxima of ~1 m at the
245   centres of the maximum load changes to zero at distances of < 500 m; observations that are
246   supported by an exact analytic solution for flexure of a floating, thin elastic plate, in which

247   constrained parameter values fall within sensible ranges.

248   Ultimately, the observations presented here provide an initial performance constraint to guide the
249   development of regional- and continent-scale ice-sheet models[37,38] to produce more accurate
250   predictions of future sea-level rise following ice-shelf collapse[7,39-41]. The process of ice-shelf
251   flexure in response to surface meltwater load changes[11], which may lead to fracture[9], is not yet
252   simulated by these models.

Methods

254   **GPS deployment and data processing.** 12 differential GPS stations were deployed in the field
255   area from mid-November 2016 to mid-January 2017 (Figs. 1b and 2, red stars). The GPS stations,
256   provided by UNAVCO, were Trimble NetR9 with Zephyr Geodetic antennas, with photovoltaic
257   power supplies. The antennas were placed on 3 m aluminum poles driven ~ 2.5 m (with a Kovacs
258   drill) into the ice at the start of the field campaign, leaving the antennas initially elevated ~ 0.5 m
259   above the ice surface. At the end of campaign, surface ablation caused some pole emergence at the
260   sites, however all antennas were still rigidly fixed with respect to the subsurface ice reference
261   frame at the bottom of the survey poles, and the poles had tilted < 5∘.

262   The L1 and L2 carrier frequency data (15 sec sample rate) recorded by the GPS receivers
263   were processed using the TRACK software package maintained by the Massachusetts Institute of
264   Technology using the GPS base station located at McMurdo Station (~15 km from the field area,
265   and operated by UNAVCO). Parameters specifying standard deviation for horizontal and vertical
266   motion used by the Kalman filter within TRACK, 30 mm of motion between samples in each
267   direction, were estimated conservatively, and variation of this choice was not found to change the
268   processed data significantly. Following the application of TRACK to determine the vertical
269   elevation time series, the data were quality checked for outliers and obvious cycle slips (10s of mm
270   displacement over time periods of < 10s of minutes), and these were replaced with interpolations.

271   Tidal displacement showing the dominant diurnal tide of McMurdo Sound with a weak
272   semidiurnal component and the familiar spring-to-neap tidal cycle was the principal vertical
273   motion in the time series. To restrict attention to only long-period monotonic vertical
274   displacements associated with load-driven ice-shelf flexure, the tidal signals from each of the 12
275   stations were removed. This was done using a least-squares estimation of pure sinusoidal variation
276   within each time series, applied with 3 dominant diurnal and 4 dominant semidiurnal frequencies
277   (K1, O1, S1, M2, S2, N2, K2) to produce the long-term vertical displacement residual presented in
278   this paper. Subsequently, the data were smoothed using a 24-hour running mean to remove other
279   lower and higher frequency signals, including non-sinusoidal signals that are nearly at the tidal
280   frequencies (e.g. diurnal multi-path error).

281   Following de-tiding and smoothing, the long-term vertical displacement residual was
282   corrected for the inverse barometer effect (IBE) using barometric data (logged every 10 mins)
283   from two AWSs located 10 - 15 km from the field area (operated by the University of Wisconsin
284   Antarctic Meteorological Research Center (AMRC), Pegasus North and Willy Field). The vertical
285   displacement coefficient for the IBE used was 0.9948 cm mb^{-1}. Because the IBE is common to all
286   stations, errors in its application have no effect on vertical displacement differences between
287   stations used to infer ice-shelf flexure.

288   Applying the time-averaging and tide removal algorithms described above to the elevation
289   time series presented in Figs. 3 and 4 renders errors due to short-term (seconds to minutes)
290   influences (due to GPS receiver effects and data processing uncertainties, and to ice-shelf

291   movements due to long-period ocean swell) to ± 10 mm; and renders errors due to long-term
292   (hours to days) effects (due to ocean tide and the IBE) to ± 50 mm. To arrive at these estimates of
293   uncertainty, we computed the standard deviation of vertical-elevation differences between pairs of
294   stations in hourly time-windows over 1944 windows in an 81-day period when all stations were
295   recording data simultaneously. The histogram of standard deviations for the 1944 hour-long time
296   windows peaked at 48 mm, suggesting that the standard deviation of errors affecting our analysis
297   is < 50 mm. Figs. 3 and 4 show 24-hour running means of relative vertical GPS displacement. We
298   expect the error associated with these running means to be $1/(\sqrt{24})$, ≈ 1/5 of the ± 50 mm estimate
299   derived from the hourly windows, or ~ ± 10 mm. It does not make sense to plot this small error
300   bracket on all of our GPS time series as they would not be visible.

301   **Pressure transducer deployment and data processing.** 8 HOBO® (U20L-01) water pressure
302   transducers, with a 0 - 9 m range and a 10-min logging interval, were deployed in and around the
303   lake study sites from mid-November 2016 until mid-January 2017 (Fig. 1b, open green circles).
304   We show water-depth data from the three transducers that were retrievable and which showed non-
305   negligible water depth changes (Figs. 3 and 4). These were located near to Ring GPS 1, WT GPS
306   1, and Rift Tip GPS 1.
307   To account for barometric pressure fluctuations, the data were corrected against air
308   pressure data from the AMRC Pegasus North AWS. The sensors have a typical water level
309   accuracy of ±3 mm and a resolution of ~2 mm (http://www.onsetcomp.com/products/data-
310   loggers/u20l-01).
311   At all sites, we initially deployed two transducers at the height of the ice surface, a fixed
312   transducer secured to an aluminium pole drilled into the ice, and a loose transducer which was to
313   slide down the pole as the ice ablated. Following ref. 26, we had hoped to calculate lake-bottom
314   ablation using this method. Here though, we just report water depths relative to the ablating lake
315   bottom. At WT GPS 1, the transducer successfully slid down the pole as the surface ablated. It
316   therefore measured the water depth relative to the lake bottom, through time (Fig. 4a, dark blue
317   line). At Ring and Rift Tip GPS 1s, however, we only have data from the height of the fixed
318   transducers (Figs 3a and b, green lines) because the loose transducers were either irretrievable
319   (Ring GPS 1) or remained stuck against the pole at the height of the fixed transducer (Rift Tip
320   GPS 1). At both Ring and Rift Tip GPS 1s, we therefore estimate lake depth relative to the lake
321   bottom using the following procedures. The fixed transducers were initially secured to their pole at
322   the lake bottom, where there was 0 m water depth. At Ring GPS 1, we measured the water depth
323   between the fixed transducer and the lake bottom (1.3 m) when we retrieved the sensors. Using
324   these data, we calculated the average lake-bottom ablation rate at Ring GPS 1 during the sensor's
325   deployment to be 20.3 mm day^{-1}, which we used in conjunction with the fixed sensor water depth
326   data (Fig. 3a, green line) to estimate water depth relative to the lake bottom (Fig. 3a, dashed dark
327   blue line). At Rift Tip GPS 1, the lake bottom was dry when we retrieved the transducers on 18
328   January. As we were unable to calculate an ablation rate for the time the lake contained water, we
329   used the ablation rate measured at Ring GPS 1 of 20.3 mm day^{-1} to correct the fixed transducer
330   data to produce an estimated depth relative to the lake bottom (Fig. 3b, dashed dark blue line). We
331   have independent evidence that this is an accurate ablation rate to use, at it gives a total ablation of
332   0.37 m over the 18 days when water was in the lake basin, we know the sensors were 0.60 m
333   above the dry lake bottom when the sensors were retrieved after a total of 41 days, requiring a dry
334   ice ablation rate of 10 mm d^{-1} for the 23 days that the sensors were out of the water, which is
335   comparable with the rate measured against other stakes in the vicinity of Rift Tip GPS 1 over the

336   summer.

337   **Time-lapse camera deployment and analysis.** A Harbortronics Cyclapse time-lapse camera
338   system, containing a Canon EOS Rebel T6i, was deployed from 25 November 2016 until 27
339   January 2017 beside Rift Tip GPS 1 (Fig. 1b, filled blue circle). It was mounted on a steel pole
340   attached to a 4-inch x 4-inch wooden stake drilled into the ice and it was programmed to take a
341   photo every 30 minutes. Following retrieval, the 3015 images were date- and time-stamped in
342   MATLAB (three of which are shown in Supplementary Fig. 1), then processed in GoPro Studio to
343   produce a movie with a frame rate of 30 sec^{-1} (Supplementary Movie 1).

344   **Seasonal net meltwater budget calculations.** The seasonal net meltwater budget, defined as the
345   total meltwater ponding volume minus the total meltwater production volume, through the
346   2016/2017 melt season, was calculated within circles of radius (r) = 250 m (area = ~2 x 10^5 m^2),
347   centred on each of the 12 GPSs (Fig. 1b, white dashed circles). Circles with this dimension were
348   chosen for various reasons. First, the maximum distance between any two GPS stations along each
349   lake transect is 500 m, so 250 m radii circles around those stations do not overlap. Second, the
350   frozen lake scars in our two partially clean lake sites, Peanut and Ring, have radii of ~250 m, and
351   thus it did not seem sensible to make the circles for meltwater budget calculations any smaller.
352   And third, using larger circles would have resulted in significant overlap between the circles, and
353   therefore, potentially similar meltwater budgets around each GPS station. We note that sensitivity
354   tests showed that changing the areas of the circles that were analysed (from r = 125 – 500 m) did
355   not change the meltwater budget trends for any of the GPS. Details of meltwater ponding and
356   meltwater production calculations are given below.

357   **Observed surface meltwater ponding calculations.** We used data collected by the Landsat 8
358   sensor to estimate areas and depths, and therefore volumes, of ponded meltwater over our study
359   region through the 2016/2017 melt season. Landsat 8 was launched in 2013 and hosts the
360   operational land imager (OLI) spectrometer, suitable for lake area and depth estimation[42,43]. Only
361   images with no cloud-cover across our four lake study sites were used. In total, 10 such images
362   between 1 November 2016 and 31 January 2017 were available (Supplementary Table 2).

363   Reflectance values were used to extract both the area and the depth of surface water using a
364   combination of bands. Landsat 8 bands 2 (blue, 450-510 nm), 4 (red, 640-670 nm), 7 (shortwave
365   infrared, 2100-2300 nm) and 8 (panchromatic, 500-680 nm) were cropped to our area of interest
366   (using Extract by Mask in ArcMap^{TM}). We used each image's metadata to convert digital numbers
367   to top-of-atmosphere (TOA) reflectance and to correct for solar elevation. These TOA reflectance
368   values represent an adequate proxy for surface reflectance[42].

369   To identify water-covered pixels, we calculated the normalized difference water index
370   adapted for ice (NDWI$_{ice}$), defined as:

371

372                    $$NDWI_{ice} = (B2 - B4 / B2 + B4) \qquad (1)$$

373

374   where B2 and B4 represent the blue and red bands respectively. Owing to the spectral dependency
375   of water reflectance, pixels covered in deeper water will have higher NDWI$_{ice}$ values. Pixels with
376   NDWI$_{ice}$ > 0.07 were assumed to be water-covered. This value is lower than that (0.12) used to
377   detect water-covered pixels in Landsat 8 in other studies[33,44], because we lowered this threshold by

9

378   the minimum amount necessary (in increments of 0.01) to include pixels that we knew to be water-
379   covered from our ground instrumentation (i.e. our 8 water pressure transducers).
380   Nine images (15 November 2016 – 25 January 2017 inclusive) were found to contain
381   water-covered pixels (Supplementary Table 2).
382   To calculate water depth for the pixels identified as being water-covered, we employed the
383   physically-based, single-band, water-depth retrieval algorithm originally based on the Bouguer-
384   Lambert-Beer law[45,46], which describes the attenuation of radiation through a water column;
385   deeper water results in higher light attenuation within the column than shallower water. The
386   expression for reflectance immediately below the water surface for optically shallow,
387   homogeneous water, $R(0-)$, is given by:

388   $$R(0-) = R\infty + (A_d - R\infty)\exp(-gz) \qquad (2)$$

389

390   where A_d is the lake bottom albedo, $R\infty$ is the reflectance of optically deep water, and the
391   coefficient g accounts for losses in upward and downward travel through the water column and
392   varies with the wavelength used[40]. Solving this equation for water depth (z) gives:

393

394   $$z = [\ln(A_d - R\infty) - \ln(R_{water} - R\infty)]/g \qquad (3)$$

395

396   where R_{water} is the reflectance of a water-covered pixel. A_d was calculated image-by-image on a
397   pixel-by-pixel basis, by taking the mean reflectance of a ring dilated by one pixel around each
398   ponded region[47,48], an improvement on previous studies that used static values across a region[46,49].
399   Some images did not contain optically deep water, and for those images, the difference between
400   using an $R\infty$ value of 0 and a value obtained from the ocean was negligible; for these reasons, an
401   $R\infty$ value of 0 was used[43]. The depth of each water-covered pixel was calculated by averaging the
402   water depths (z) derived from Landsat 8's bands 4 and 8 (ref 42). The values for g (0.7507 for band
403   4 and 0.3817 for band 8) were taken from ref. 42. This method of calculating water depth makes
404   several assumptions, including: the lake substrate is homogenous and the impact of any dissolved
405   matter in the water on absorption is negligible; and there is no scattering of light from the lake
406   surface associated with roughness due to wind[46]. We appreciate that the first assumption may be
407   particularly problematic in our study area due to the large amounts of fine debris that accumulates
408   in the areas where water ponds.
409   Finally, after water depth was calculated, dry debris that was falsely identified as water,
410   was removed from the images. As dry debris is known to have high band 7 and low band 2
411   reflectance values (whereas water has low band 7 and high band 2 reflectance values), this was
412   done by masking out band 7 pixels with reflectance > 0.4 and band 2 pixels with reflectance < 0.2.
413   These thresholds were determined by performing a combination of visual analysis and inspection
414   of the reflectance values in bands 2 and 7 for water and debris. A blue-band threshold has similarly
415   been employed in other studies to remove pixels falsely identified as water[50,51], but we are not
416   aware of the shortwave infrared band having previously been used for a similar purpose.
417   We do not have errors on our meltwater volume calculations as due to our method of
418   determining a suitable $NDWI_{ice}$ threshold (see above), the errors on our water-covered pixel areas
419   are assumed to be negligible, and the average depth error across multiple water-covered pixels
420   using bands 4 and 8 has been shown to be zero (because positive and negative errors cancel out)[42].

421 **Surface meltwater production calculations.** We used a PDD model to calculate meltwater
422 production during the 2016/2017 melt season. Two PDD factors, one for dirty, low-albedo, ice,
423 and one for clean, high-albedo, ice, were derived empirically from our 2-m air temperature data
424 and in-situ ablation measurements. Air temperature data were logged every 15 minutes at our
425 AWS, which was installed from 22 November 2016 to 27 January 2017 in the centre of Rift Tip
426 lake (Fig. 1b, yellow star). Surface ablation was measured against each of the 12 GPS antenna
427 poles, between the time of their installation in November 2016, and their retrieval in late January
428 2017. The 12 measurements clearly split into two groups; a dirty ice group (Rift Tip GPSs 1 and 2,
429 and WT GPS 1) with melt rates > 12 mm w.e. day^{-1}, and a clean ice group with melt rates < 4 mm
430 w.e. day^{-1}. Our dirty ice and clean ice PDD factors are the mean of the PDD factors for the three
431 dirty stake locations (47.5 mm w.e. $^{\circ}$C^{-1} day^{-1}) and the 9 clean locations (6.4 mm w.e. $^{\circ}$C^{-1} day^{-1}),
432 respectively. The Standard Errors of these means are 9.0 and 0.9 mm w.e. $^{\circ}$C^{-1} day^{-1}, respectively,
433 i.e. 19% and 13% of the respective PDD factors.
434   To apportion pixels within each circle around each GPS into two categories, dirty and
435 clean, we applied the MATLAB function graythresh to the band 8 TOA reflectance values from
436 the nine Landsat 8 images for the 2016/2017 melt season that our analysis had already shown to
437 include of surface meltwater (Supplementary Fig. 3 and Supplementary Table 2). Using Otsu's
438 method, this function chooses the threshold value that minimizes the intra-class variance of the
439 black and white pixels. This dynamic thresholding approach is empirical, and justified by the
440 observation that dirty pixels are relatively darker than clean pixels at wavelengths in the solar
441 reflective part of the spectrum. Dynamic thresholding has been used in a variety of previous
442 studies[49] to categorise MODIS images into water and not water covered areas. We note that it was
443 not possible to simply choose a threshold by eye as the histograms of TOA reflectance were
444 generally not indicative of a bimodal distribution. Once chosen, the threshold was used to produce
445 a binary image of clean (i.e. white) and dirty (i.e. black) pixels and, for quality control, they were
446 visually inspected and compared to the true colour Landsat 8 images and histograms
447 (Supplementary Fig. 3).
448   From these binary images, the percentage of dirty versus clean pixels in each circle of each
449 image was calculated (Supplementary Fig. 3). As daily volumes of calculated meltwater
450 production through the season were required, we linearly interpolated these percentage values to
451 daily values between each of the nine image dates. Finally, for each day 2016/2017 melt season,
452 the clean and dirty PDD factors were applied proportionately to each circle, and daily volumes of
453 total meltwater production were calculated. To calculate the errors for the volumes of meltwater
454 production, we assume that the errors associated with the apportioning of dirty versus clean pixels
455 are negligible, and use the mean Standard Error of the means of two PDD factors (16%).

456 **Exact analytic solution for flexure of a thin elastic plate.** Flexure of an ice shelf subject to
457 changing surface-meltwater loads can be represented, for purpose of estimating stress magnitudes,
458 using an analytic solution based on thin elastic (Kirchhoff) plate theory[11,53]. Following ref. 10, we
459 use an azimuthally-symmetric solution valid for $r > 0$ to the thin-elastic-plate flexure equation
460 (also known as the Kirchoff-Love equation, but modified to account for buoyancy associated with
461 ocean water below the thin plate) in which disk-shaped meltwater loads, or anti-loads (associated
462 with the drainage of lakes), are confined within a region $r \leq R$ using polar coordinates r, θ, and
463 where R is the radius of the lake or drained-lake. The vertical displacement of the elastic plate,

464     $\eta(r)$, for $0 \leq r \leq \infty$, is expressed in terms of Kelvin-Bessel functions (as derived by ref. 54), and
465   displayed in ref. 11. An undeflected ice shelf at a large distance (i.e. $r \leq \infty$) is assumed, which is
466   appropriate because the grounding lines and ice front are ≥ 2 km from all lake centres.

467   Values for the three parameters: lake radius (R); effective ice thickness (H); and Young's
468   Modulus (E), were varied to produce the best match between the analytic solution and measured
469   lake-centre deflection for Ring Site (Fig. 5; Supplementary Table 1). Having identified suitable
470   parameter values for H and E, these were held constant, while R was varied (by 25 m increments)
471   to find a best match between the analytic solution and measured lake-centre deflection for Rift Tip,
472   WT and Peanut Sites (Supplementary Fig. 2). Following ref. 10, the other parameter values are
473   kept constant in this study: $\rho_{sw} = 1028$ kg m^{-3} is the density of seawater, $\rho_{ice} = 910$ kg m^{-3} is the
474   density of ice, $\rho_{fw} = 1028$ kg m^{-3} is the density of fresh water, $g = 9.81$ m s^{-2} is the acceleration of
475   gravity, and $\nu = 0.3$ is the Poisson ratio. For simplicity, and because debris layers were relatively
476   thin (order 10s of cm), we did not account for changes in the effective density of ice due to debris
477   content. Input to the analytic solution is a disk-shaped meltwater load removal, taken as the
478   calculated seasonal net meltwater budget for each site (Figs. 3 and 4).

479   We use an elastic treatment of flexure stresses induced after lake drainage under the
480   assumption that the timescale of lake drainage via overflow is relatively short compared to the
481   Maxwell time[10,11]. However, in reality, as it may take a year or more for a lake to fill, a viscous
482   response of the ice shelf will be present too[12,20,53]. The maximum flexure stresses implied by the
483   elastic solution therefore represent maximum upper bounds; with a viscoelastic model[12,20],
484   modelled deflections at all GPS stations, including the lake centre stations, would be lower, and
485   the flexure stresses would also all be lower. Additionally, using a viscoelastic model, the ice-shelf
486   flexural response to the change in lake load would be even more local than that observed with the
487   current analytic solution for flexure of a thin elastic plate, which our GPS data would support.

488   **Data availability.** The field-derived GPS (https://doi.org/10.15784/601107) and AWS
489   (https://doi.org/10.15784/601106) data are archived at the USAP Data Center. Landsat 8 tiles can
490   be obtained from Earth Explorer (http://earthexplorer.usgs.gov/.)

491

492   References

493   1. Glasser, N. F. & Scambos, T. A. A structural glaciological analysis of the 2002 Larsen Ice Shelf
494   collapse. *J. Glaciol.,* **54**(184), 3–16, (2008).

495   2. Langley, E. S., Leeson, A. A., Stokes, C. R. & Jamieson, S. S. R. Seasonal evolution of
496   supraglacial lakes on an East Antarctic outlet glacier. *Geophys. Res. Lett.* **43,** 8563–8571 (2016).

497   3. Kingslake, J., Ely, J. C., Das, I. & Bell, R. E. Widespread movement of meltwater onto and
498   across Antarctic ice shelves**,** *Nature,* **544,** 349–352 (2017).

499   4. Lenaerts, J. T. M. *et al.* Meltwater produced by wind-albedo interaction stored in an East
500   Antarctic ice shelf. *Nat. Clim. Chang.* **7,** 58–62 (2017).

501   5. Bell, R., Banwell, A. F., Trusel, L., Kingslake, J. 2018, Antarctic Surface Hydrology & Impacts
502   on Ice Sheet Mass Balance, *Nat. Clim. Chan. Perspectives,* **8**(12), 1044–1052, doi:
503   10.1030/s41558-018-0326-3

504 6. Phillips, H. A. Surface meltstreams on the Amery Ice Shelf, East Antarctica. Ann. Glaciol. 27,
505 177–181, (1998), https://doi.org/10.3189/1998AoG27-1-177-181.

506 7. Scambos, T. A., Bohlander, J. A., Shuman, C. U. & Skvarca, P. Glacier acceleration and
507 thinning after ice shelf collapse in the Larsen B embayment, Antarctica. *Geophys. Res. Lett*. **31,**
508 L18402 (2004).

509 8. Van den Broeke, M., Strong surface melting preceded collapse of Antarctic Peninsula ice shelf.
510 *Geophys. Res. Lett*., **32**(12), L12815, (2005).

511 9. Scambos, T.A *et al*. Ice shelf disintegration by plate bending and hydro-fracture: satellite
512 observations and model results of the 2008 Wilkins Ice Shelf break-ups. *Earth and Planetary*
513 *Science Letters*, **280**, (2009).

514 10. Banwell A. F., MacAyeal D. R. & Sergienko O. V. Breakup of the Larsen B Ice Shelf
515 triggered by chain reaction drainage of supraglacial lakes. *Geophys. Res. Lett.,* **40**, L02502, (2013).

516 11. MacAyeal, D. R. & Sergienko, O. V. Flexural dynamics of melting ice shelves, *Ann. Glaciol.,*
517 **54**(63), 1–10, (2013).

518 12. Banwell A. F. & MacAyeal D. R. Ice-shelf fracture due to viscoelastic flexure stress induced
519 by fill/drain cycles of supraglacial lakes. *Antarct. Sci.,* **27**, 587–597, (2015).

520 13. Beltaos, S., Collapse of floating ice covers under vertical loads: Test data vs. theory, *Cold Reg.*
521 *Sci. Technol.,* 34, 191–207 (2002).

522 14. Scambos, T. A., Hulbe, C., Fahnestock, M. & Bohlander, J. The link between climate warming
523 and break-up of ice shelves in the Antarctic Peninsula. *J. Glaciol.* **46,** 516–530 (2000).

524 15. Pritchard, H. D. *et al.* Antarctic ice-sheet loss driven by basal melting of ice
525 shelves. *Nature* **484**, 502–505 (2012).

526 16. Liu *et al.* Ocean-driven thinning enhances iceberg calving and retreat of Antarctic ice shelves,
527 *PNAS*, **112**(11), 3263–3268 (2015).

528 17. Paolo, F. S., Fricker, H. A & Padman L. Ice sheets. Volume loss from Antarctic ice shelves is
529 accelerating. *Science*. **348**(6232):327-31 doi: 10.1126/science.aaa0940 (2015).

530 18. Reese, R. Gudmundsson, G. H. Levermann, A & Winklemann, R. The far reach of ice-shelf
531 thinning in Antarctica, *Nature Climate Change***, 8**, 53–57 (2018).

532 19. Pattyn, F., C. *et al*., The Greenland and Antarctic ice sheets under 1.5 °C global warming, *Nat.*
533 *Clim. Chan*., doi:10.1038/s41558-018-0305-8, (2018).20. MacAyeal, D.R., Sergienko, O.V. and
534 Banwell, A.F. A model of viscoelastic ice-shelf flexure. *J. Glaciol.*, **61**, 635-645, (2015).

535 21. Banwell, A. F. *et al.* Calving and rifting on the McMurdo Ice Shelf, Antarctica. *Ann. Glaciol.*
536 1-10, (2017).

537 22. Glasser, N. F., Goodsell, B., Copland, L. & Lawson, W. Debris characteristics and ice-shelf
538 dynamics in the ablation region of the McM Ice Shelf, Antarctica. *J. Glaciol*., **52**(177), 223–234,
539 (2006).

540 23. MacAyeal, D.R., *et al.* Diurnal Seismicity Cycle Linked to Subsurface Melting on an Ice
541 Shelf, *Ann. Glaciol*. doi: 10.1017/aog.2018.29 (2018).

542 24. Rack, W. Haas, C & Langhorne, P. J. Airborne thickness and freeboard measurements over the
543 McM Ice Shelf, Antarctica, and implications for ice density. J. *Geophys. Res. Oceans*, **118**, 5899–
544 5907, (2013).

545 25. Campbell, S., Courville, Z., Sinclair, S., & Wilner, J. Brine, englacial structure and basal
546 properties near the terminus of McMurdo Ice Shelf, Antarctica. *Ann. Glaciol,* **58**(74), 1-11, (2017).

547 26. Tedesco, M. et al. Measurement and modeling of ablation of the bottom of supraglacial lakes
548 in western Greenland. *Geophys. Res. Lett.* **39**, L02502 (2012).

549 27. Das, S. B. *et al.* Fracture propagation to the base of the Greenland ice sheet during supraglacial
550 lake drainage, *Science*, 320, 778–781 (2008).

551 28. Tedesco, M. et al. Ice dynamic response to two modes of surface lake drainage on the
552 Greenland ice sheet. *Environ. Res. Lett.* **8**, 34007 (2013).

553 29. Gold, L.W., 1977. Engineering properties of freshwater ice. *J. Glaciol* **19**(81), 197–212.

554 30. Van der Veen C. J. Fracture mechanics approach to penetration of surface crevasses on
555 glaciers. *Cold Reg. Sci. Technol.*, **27**(1), 31–47 (1998).

556 31. Albrecht, T. & Levermann, A. Fracture field for large-scale ice dynamics, *J. Glaciol.*, **58**(207),
557 165–176 (2012).

558 32. Banwell A. F. Glaciology: Ice-shelf stability questioned. *Nature*, **544**, 306-307 (2017).

559 33. Bell, R. E. *et al.* Antarctic ice shelf potentially stabilized by export of meltwater in surface
560 river. *Nature,* **544**(7650):344-348 (2017).

561 34. Robel, A. A. Thinning sea ice weakens buttressing force of iceberg mélange and promotes
562 calving. *Nat. Commun.* **8,** 14596, (2017).

563 35. Rignot, E., Mouginot, J, & Scheuchl, B Ice flow of the Antarctic Ice Sheet, *Science*,
564 333(6048), 1427–1430 (2011).

565 36. Trusel, L. D. *et al.* Divergent trajectories of Antarctic surface melt under two twenty- first-
566 century climate scenarios. *Nat. Geosci.* **8,** 927–932 (2015).

567 37. Pollard, D. DeConto, R. M. & Alley, R. B. Potential Antarctic Ice Sheet retreat driven by
568 hydrofracturing and ice cliff failure. *Earth Planet. Sci. Lett.* **412**, 112–121 (2015)

569 38DeConto, R. M. & Pollard, D. Contribution of Antarctica to past and future sea-level rise.
570 *Nature* **531,** 591–597 (2016).

571 39. De Rydt, J., Gudmundsson, G., Rott, H. & Bamber, J. Modeling the instantaneous response of
572 glaciers after the collapse of the Larsen B Ice Shelf. *Geophys. Res. Lett.* **42**, 5355–5363 (2015).

573 40. Church, J. A. et al. in *Climate Change 2013: The Physical Science Basis* (eds Stocker, T. F. et
574 al.) 1137–1177 (IPCC, Cambridge Univ. Press, 2013).

575 41. Fürst, J. J. *et al.* The safety band of Antarctic ice shelves. *Nat. Clim. Change,* 6, 2014–2017
576 (2016).

577 42. Pope, A. *et al.* Estimating supraglacial lake depth in West Greenland using Landsat 8 and
578 comparison with other multispectral methods. *Cryosphere* **10**(1): 15-27, (2016).

579 43. Macdonald, G. J., Banwell, A. F. & MacAyeal, D.R. Seasonal evolution of supraglacial lakes
580 on a floating ice tongue, Petermann Glacier, Greenland. *Ann. Glaciol.*, 1 -10, (2018).

581 44. Yang, K. & Smith, L. C., Supraglacial streams on the Greenland Ice Sheet delineated from
582 combined spectral-shape information in high-resolution satellite imagery. *IEEE Geosci. Remote*
583 *Sens. Lett.* **10** (4):801–805, (2013).

584 45. Philpot, W. D. Bathymetric mapping with passive multispectral imagery. *Appl. Opt.*, **28**(8),
585 1569–1578, (1989).

586 46. Sneed, W. A. & Hamilton, G. S. Evolution of melt pond volume on the surface of the
587 Greenland Ice Sheet, *Geophys. Res. Lett.*, **34**(3), L03501, (2007).

588 47. Arnold, N. S., Banwell, A. F, & Willis, I. C. High-resolution modelling of the seasonal
589 evolution of surface water storage on the Greenland Ice Sheet, *Cryosphere*, **8**, 1149-1160, (2014).

590 48. Banwell, A.F. *et al.* Supraglacial lakes on the Larsen B ice shelf, Antarctica, and at Paakitsoq,
591 West Greenland: A comparative study. *A. Glaciol.* **55**, 1-8, (2014).

592 49. Morriss, B. F. *et al.* A ten-year record of supraglacial lake evolution and rapid drainage in
593 West Greenland using an automated processing algorithm for multispectral imagery. *Cryosphere*
594 **7**, 1869–1877, (2013).

595 50. Doyle, S. H. *et al.* Ice tectonic deformation during the rapid in situ drainage of a supraglacial
596 lake on the Greenland Ice Sheet, *Cryosphere*, **7**, 129–140, (2013).

597 51. Fitzpatrick, A. A. W. *et al*. A decade (2002–2012) of supraglacial lake volume estimates across
598 Russell Glacier, West Greenland, *Cryosphere*, **8**, 107 – 121 (2014).

599 52. Pavelsky, T. M. & Smith L. C. Remote sensing of hydrologic recharge in the Peace-Athabasca
600 Delta, Canada, *Geophys. Res. Lett.*, **35**, L08403, (2008).

601 53. Kerr, A. D. The bearing capacity of floating ice plates subjected to static or quasi-static loads,
602 *J. Glaciol.*, **17**(76), 229–268, (1976).

603 54. Lambeck, K., and Nakiboglu, S. M. Seamount loading and stress in the ocean lithosphere, *J.*
604 *Geophys. Res*., **85**(B11), 6403–6418 (1980).

605

Acknowledgements

617

Author Contributions

619 A.F.B. led the field project and the preparation of the manuscript. I.C.W. ran the PDD melt model.
620 G.J.M. calculated meltwater ponding volumes and determined brightness thresholds for dirty
621 versus clean ice from satellite imagery. D.R.M. processed the GPS data. A.F.B. and D.R.M.
622 implemented and ran the analytic thin elastic plate over seawater solution. All authors (A.F.B.,
623 I.C.W., G.J.M., B.G., and D.R.M.) were involved in the planning and execution of the field
624 campaign and in the drafting of the manuscript.

625

Competing interests

The authors declare no competing interests.

Figure captions

Fig. 1 | **Study site on the McMurdo Ice Sheet in vicinity of McMurdo Station and Scott Base.** The background of both (a) and (b) is a WorldView-2 image (©2016, DigitalGlobe) dated 2 December 2016. In (a), the green star in the top-left inset indicates the location of the McMIS, and the black arrow indicates the local ice flow direction and speed (~335° True at ~28 m a^{-1}), based on our own GPS velocity data from the 2016/2017 austral summer. The red box indicates the location of our study site, shown in (b), in which the four lake sites are labelled. At each lake site, the locations of three GPS stations are marked with red stars (labelled 1 to 3, where 1 is closest to the lake centre and 3 is furthest away). Green open circles mark the locations of pressure transducers; data from three of these are shown in Figs. 3 and 4. A yellow star marks the location of the automatic weather station (AWS), and a blue circle marks the location of a time-lapse camera (used to produce Supplementary Movie 1 and Supplementary Fig. 1). The dashed-white circles of $r = 250$ m, centred on each of the 12 GPSs, show the areas where the seasonal meltwater budget was calculated. (N.B. Rift Tip lake was originally named in a previous (2015/2016) fieldwork season, when it was at the end of a rift. Although this rift has since propagated westwards by ~3 km (ref. 21), we have kept the original name.)

Fig. 2 | Aerial and ground views of the Ring lake site. The aerial view photo in (a) was taken on 18 January 2017, after the lake in the dirty, low topographic area near to GPS 1 had almost completely drained (Fig. 3a, top plot). A pedestalled, frozen lake scar can be seen in the distance (centred on GPS 3). The red box marks the spot where the photo in (b) was taken. The ground view photo in (b) was taken from the dirty, topographically-low area, looking towards the lake scar in the background, with a person for scale.

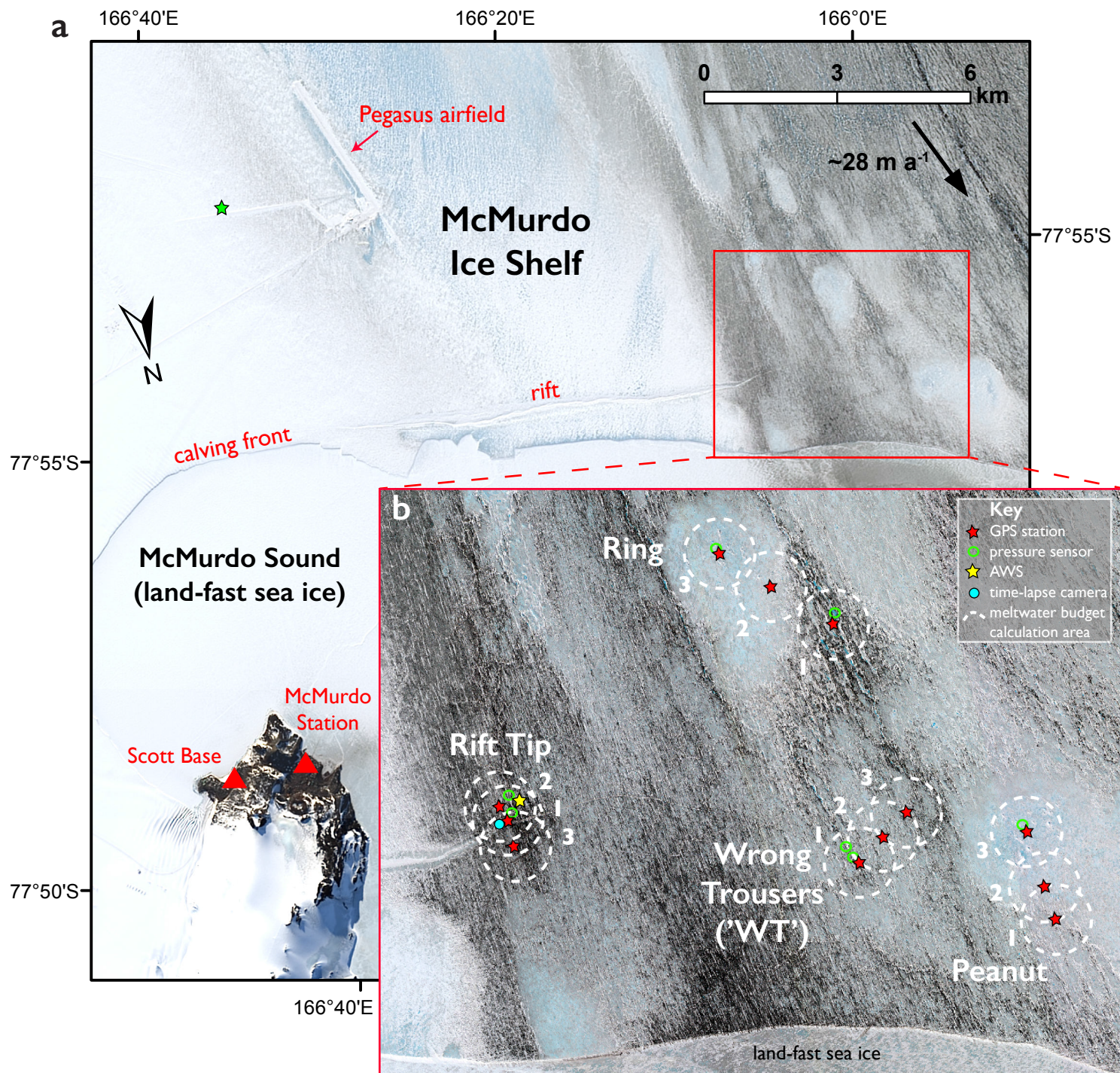**Fig. 3 | Vertical ice shelf displacement with water depths and seasonal meltwater budgets for Ring and Rift Tip lake sites.** (a) is for Ring, and (b) is for Rift Tip. For each site, the top three plots show the vertical ice-shelf displacement (relative to arbitrary elevation) from three GPS stations. The first red dot above each time series shows when GPS 1 reaches its highest elevation, before reaching its lowest elevation, shown by a second red dot. The third red dot indicates when GPS 1 reaches its highest elevation during the whole time period. Numbers next to red arrows (which depict direction of movement) are the total vertical deflections, and deflection rates, measured by each GPS over the two respective time periods between the first and second red dots, and the second and third red dots. Some of the elevation data for Rift Tip GPS 1 are missing so are linearly interpolated (dashed-red line). The fourth plot for each lake site shows water depth data from a pressure sensor near to each GPS 1. Water depths relative to lake bottom were estimated from sensors fixed at constant heights (see Methods). The bottom three plots at each site show the calculated seasonal meltwater budgets around each GPS station. The black lines (and grey shading) show cumulative volumes (and errors) of meltwater production calculated by a PDD model; light blue dots show the measured volumes of meltwater ponding from 9 cloud-free
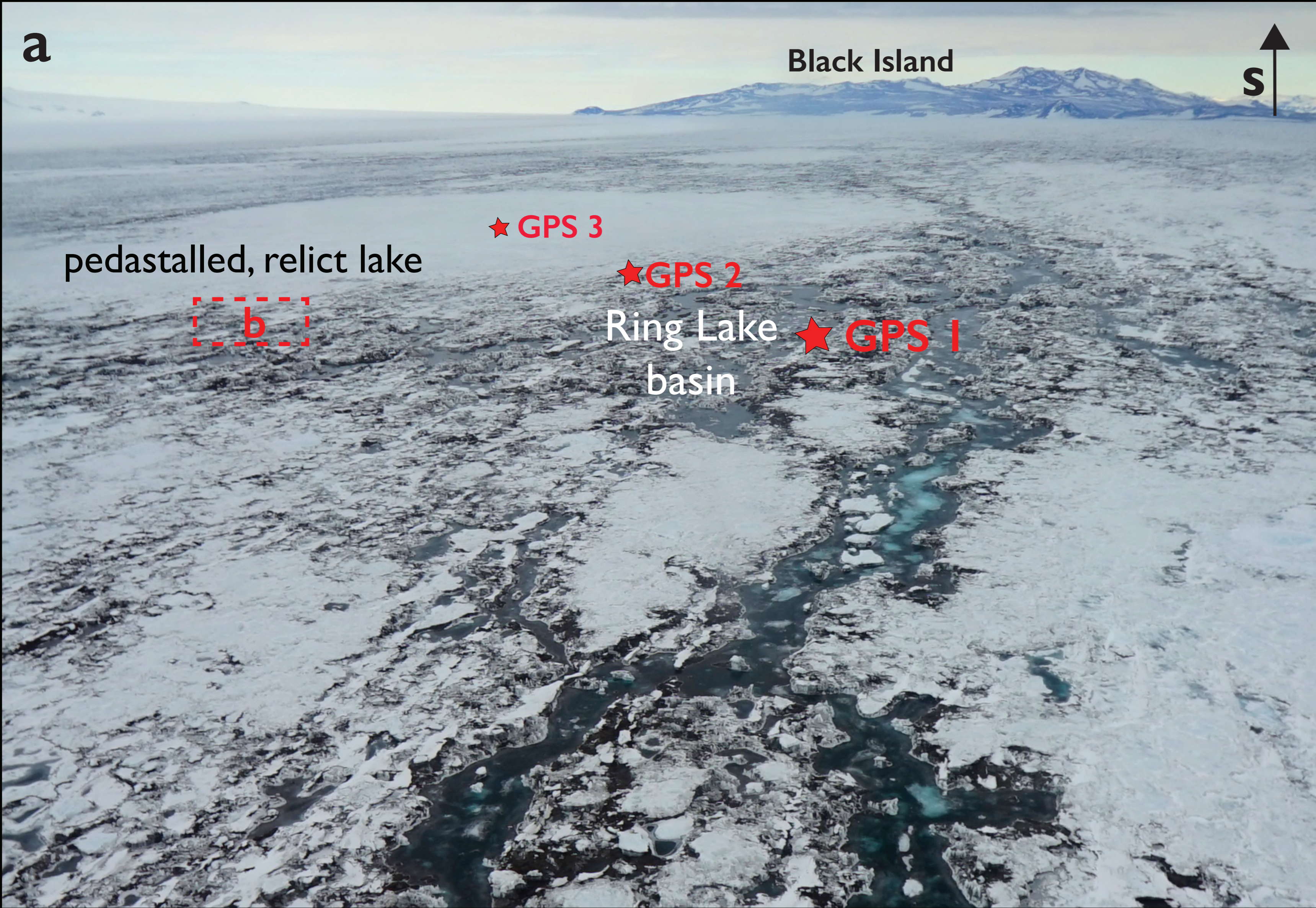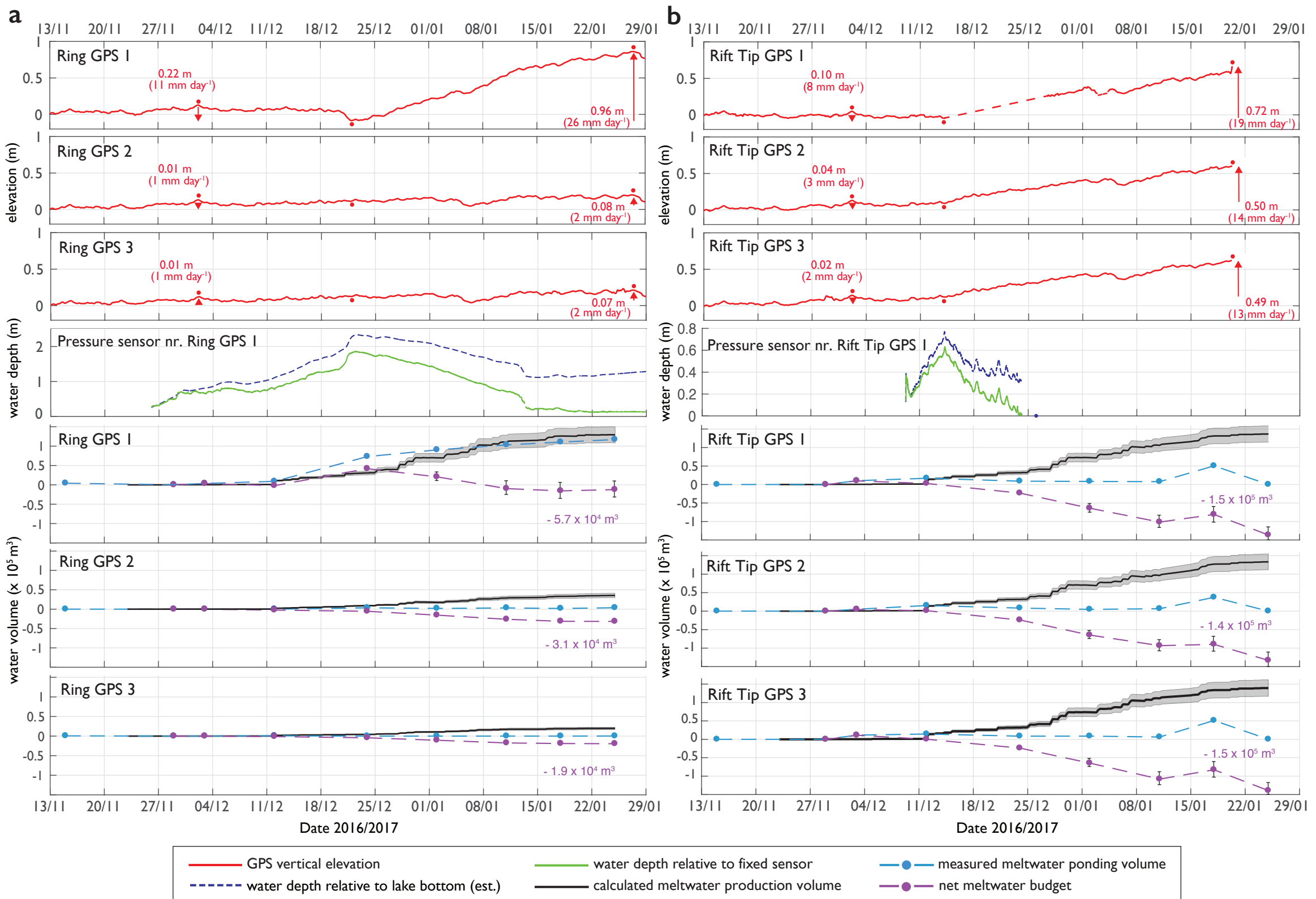
16

668   Landsat 8 images (see Supplementary Table 2 for image dates), and the dashed-light blue lines
669   show these data linearly interpolated between the image dates; purple dots (and whiskers) show
670   the net meltwater budget (and errors) on each image date, and the dashed-purple lines show these
671   data linearly interpolated between the dates. Purple numbers next to the net meltwater budget plots
672   refer to the seasonal net meltwater budgets, each defined as the maximum minus minimum net
673   meltwater budget during the melt season, which are all negative. See Fig. 1 for GPS and water-
674   depth sensor locations, and Methods for details of GPS and water-depth data processing, and
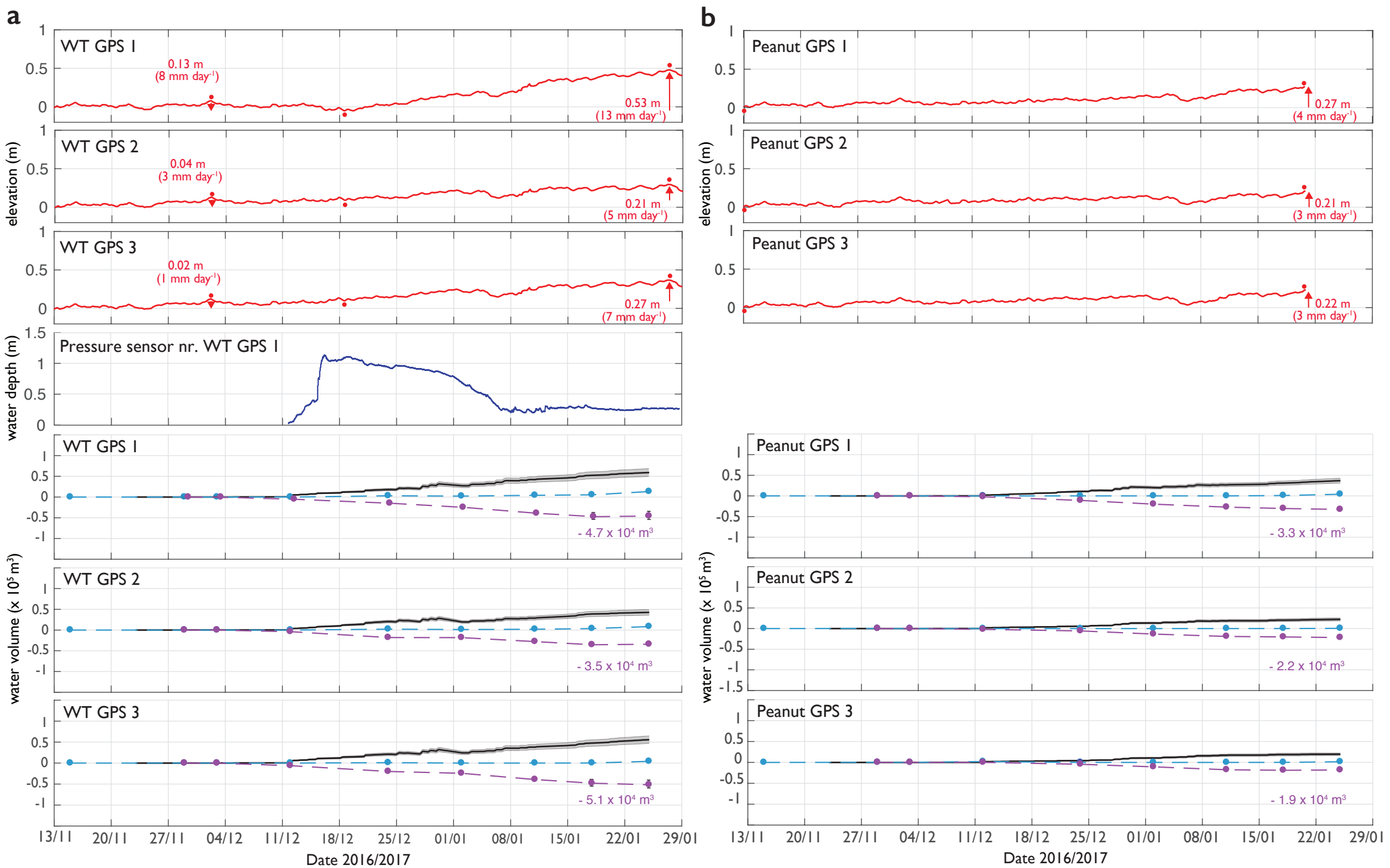675   meltwater budget and error calculations.

676   **Fig. 4 | Vertical ice shelf displacement with water depths and seasonal meltwater budgets for**
677   **WT and Peanut lake sites.** (a) is for WT and (b) is for Peanut. For each site, the top three plots
678   show the vertical ice-shelf displacement (relative to arbitrary elevation) from three GPS stations.
679   The first red dot above each time series shows when GPS 1 reaches its highest elevation, before
680   reaching its lowest elevation, shown by a second red dot. The third red dot indicates when GPS 1
681   reaches its highest elevation during the whole time period. Numbers next to red arrows (which
682   depict direction of movement) are the total vertical deflections, and deflection rates, measured by
683   each GPS over the two respective time periods between the first and second red dots, and the
684   second and third red dots. The fourth plot for each lake site shows water depth data from a
685   pressure sensor near to each GPS 1. The bottom three plots for each site show the calculated
686   seasonal net meltwater budgets around each GPS station. The black lines (and grey shaded areas)
687   show cumulative volumes of meltwater production (and errors) calculated by a PDD model; light
688   blue dots show the measured volumes of meltwater ponding from 9 cloud-free Landsat 8 images
689   (see Supplementary Table 2 for image dates), and the dashed-light blue lines show these data
690   linearly interpolated between the image dates; purple dots (and whiskers) show the net meltwater
691   budget (and errors) on each image date, and the dashed-purple lines show these data linearly
692   interpolated between the dates. Purple numbers next to the net meltwater budget plots refer to the
693   seasonal net meltwater budgets, each defined as the maximum minus minimum net meltwater
694   budget during the melt season, which are all negative. See Fig. 1 for GPS and water depth sensor
695   locations, and Methods for details of GPS and water-depth data processing, and meltwater budget
696   and error calculations.

697   **Fig. 5 | Vertical ice shelf deflection and stresses associated with the drainage of Ring Lake.**
698   Vertical ice-shelf deflection (orange line), as a function of distance from lake centre, is computed
699   by an exact analytic solution for thin elastic plate flexure above seawater, in response to the
700   drainage of Ring lake (of volume 5.7 x 10^4 m^3, equal to the calculated seasonal net meltwater
701   budget within a 250 m radius of Ring lake GPS 1, Fig. 3a). This result shows the best match
702   between the analytic solution and the measured deflection at Ring lake's centre (i.e. GPS 1) and
703   uses the following parameter values: $R = 125$ m, $H = 10$ m, and $E = 1$ GPa. The locations of GPSs
704   1, 2 and 3 (960 m from the lake centre) are indicated. The associated stresses (radial (red line),
705   azimuthal (blue line), and von-Mises (green line) as a function of distance from lake centre),
706   shown in (b), are all evaluated at the upper ice-shelf surface.

a

166°40'E 166°20'E 166°0'E

0 3 6 km

~28 m a⁻¹

Pegasus airfield

McMurdo
Ice Shelf

77°55'S

N

rift

calving front

77°55'S

McMurdo Sound
(land-fast sea ice)

McMurdo
Station

Scott Base

77°50'S

166°40'E

b

Key
★ GPS station
○ pressure sensor
★ AWS
● time-lapse camera
- - - meltwater budget
       calculation area

Ring

3

2

1

Rift Tip

2
1
3

Wrong
Trousers
('WT')

3

2

1

3

2

1

Peanut

land-fast sea ice

a — Black Island · S · pedastalled, relict lake · ★ GPS 3 · ★ GPS 2 · Ring Lake basin · ★ GPS 1 · b

b — pedastalled, relict lake

a

Ring GPS 1
0.22 m (11 mm day⁻¹)
0.96 m (26 mm day⁻¹)

Ring GPS 2
0.01 m (1 mm day⁻¹)
0.08 m (2 mm day⁻¹)

Ring GPS 3
0.01 m (1 mm day⁻¹)
0.07 m (2 mm day⁻¹)

Pressure sensor nr. Ring GPS 1

Ring GPS 1
− 5.7 × 10⁴ m³

Ring GPS 2
− 3.1 × 10⁴ m³

Ring GPS 3
− 1.9 × 10⁴ m³

Date 2016/2017

b

Rift Tip GPS 1
0.10 m (8 mm day⁻¹)
0.72 m (19 mm day⁻¹)

Rift Tip GPS 2
0.04 m (3 mm day⁻¹)
0.50 m (14 mm day⁻¹)

Rift Tip GPS 3
0.02 m (2 mm day⁻¹)
0.49 m (13 mm day⁻¹)

Pressure sensor nr. Rift Tip GPS 1

Rift Tip GPS 1
− 1.5 × 10⁵ m³

Rift Tip GPS 2
− 1.4 × 10⁵ m³

Rift Tip GPS 3
− 1.5 × 10⁵ m³

Date 2016/2017

Legend:
— GPS vertical elevation
-- water depth relative to lake bottom (est.)
— water depth relative to fixed sensor
— calculated meltwater production volume
● measured meltwater ponding volume
● net meltwater budget

a

WT GPS 1
0.13 m (8 mm day⁻¹)
0.53 m (13 mm day⁻¹)

WT GPS 2
0.04 m (3 mm day⁻¹)
0.21 m (5 mm day⁻¹)

WT GPS 3
0.02 m (1 mm day⁻¹)
0.27 m (7 mm day⁻¹)

Pressure sensor nr. WT GPS 1

WT GPS 1
− 4.7 x 10⁴ m³

WT GPS 2
− 3.5 x 10⁴ m³

WT GPS 3
− 5.1 x 10⁴ m³

b

Peanut GPS 1
0.27 m (4 mm day⁻¹)

Peanut GPS 2
0.21 m (3 mm day⁻¹)

Peanut GPS 3
0.22 m (3 mm day⁻¹)

Peanut GPS 1
− 3.3 x 10⁴ m³

Peanut GPS 2
− 2.2 x 10⁴ m³

Peanut GPS 3
− 1.9 x 10⁴ m³

elevation (m)
water depth (m)
water volume (x 10⁵ m³)

Date 2016/2017

Legend:
— GPS vertical elevation
–– water depth relative to lake bottom
— calculated meltwater production volume
•– measured meltwater ponding volume
•– net meltwater budget

a

vertical deflection

vol. meltwater unloaded = 5.7 x 10⁴ m³

← lake edge (*r* = 125 m)

GPS 1

GPS 2

GPS 3
(960 m)

b

radial stress
azimuthal stress
von Mises stress